Journal of Colloid and Interface Science 692 (2025) 137528

Contents lists available at ScienceDirect

Journal of Colloid And Interface Science

journal homepage: www.elsevier.com/locate/jcis

Regular Article

Boosting electrochemical CO_2 reduction by strong electronic interaction at the interface of Bi/SnO_2 heterostructures

Zeyu Wang [a], Yaling Jia [a,*], Shangqing Zhao [a], Huiling Zheng [a], Antony Rajendran [b], Wen-Ying Li [a,*]

[a] State Key Laboratory of Clean and Efficient Coal Utilization, Taiyuan University of Technology, Taiyuan 030024, China
[b] Department of Chemistry, Mepco Schlenk Engineering College (Autonomous), Sivakasi 626005 Tamil Nadu, India

GRAPHICAL ABSTRACT

A novel *p–p* orbital coupling effect between dual *p*-block metals catalyst Bi/SnO_2 was proposed, which can induce strong electronic interaction at the interface of Bi/SnO_2 that exhibited a maximum formate Faraday efficiency of 90.5% and the partial current density of formate is 17.1 mA cm^{-2}.

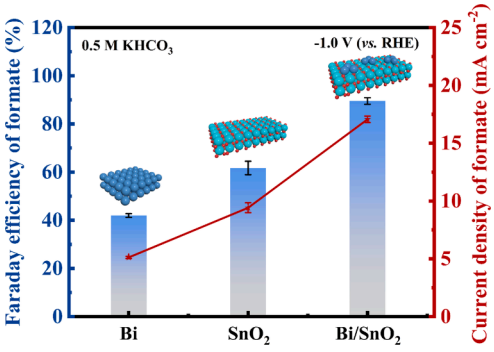

ARTICLE INFO

Keywords:
CO_2 adsorption
Electronic coupling effect
Dual *p*-block metal catalysts
Bi/SnO_2 interface

ABSTRACT

SnO_2-based materials are promising electrocatalysts for the conversion of CO_2 to formate however increasing their activity further is challenging due to the suboptimal CO_2 adsorption and activation capacity. The interfacial engineering has proven effective in modulating the electronic structure and adsorption behavior of electrocatalysts. Herein, a heterostructure Bi/SnO_2 was constructed for the CO_2 electroreduction to formate in which a formate Faraday efficiency of 94.9% and single-pass carbon efficiency of 40.3% were achieved at −1.0 V versus reversible hydrogen electrode in 1.0 M KOH. During a 30-hour stability test, the current density was nearly constant without a significant decrease while the formate Faraday efficiency was maintained around 90%. This remarkable activity is attributed to the strong electronic interaction arising from *p–p* orbital coupling at the Bi/SnO_2 interface, according to the experimental and theoretical investigations. The computational insights suggest that the *p–p* orbital coupling promotes the electron transfer from Bi to SnO_2 and optimizes the adsorption strength of the intermediate (*OCHO) to enhance the catalytic activity. The formation of *OCHO during formate generation was confirmed by the *in situ* attenuated total reflectance surface-enhanced infrared absorption

* Corresponding authors.
E-mail addresses: jiayaling@tyut.edu.cn (Y. Jia), ying@tyut.edu.cn (W.-Y. Li).

https://doi.org/10.1016/j.jcis.2025.137528
Received 16 January 2025; Received in revised form 24 March 2025; Accepted 5 April 2025
Available online 5 April 2025

spectroscopy. This work might contribute key insights into the mechanisms underlying activity enhancement via strong electronic interaction between dual *p*-block metal catalysts.

Nomenclature

Abbreviation

ATR-SEIRAS	Attenuated total reflectance surface-enhanced infrared absorption spectroscopy
CEE	Cathodic energy efficiency
DFT	Density functional theory
EDS	Energy dispersive spectroscopy
ECSA	Electrochemical active surface area
GC	Gas chromatograph
HPLC	High performance liquid chromatograph
LSV	Linear sweep voltammetry
PDOS	Projected density of states
RDS	Rate-determining step
SI	Supporting information
TEM	Transmission electron microscopy
V_O	Oxygen vacancies
XPS	X-ray photoelectron spectroscopy
CO_2-TPD	Temperature-programmed desorption of CO_2
CV	Cyclic voltammetry
ECO_2RR	Electrocatalytic CO_2 reduction reaction
EIS	Electrochemical impedance spectroscopy
FE	Faraday efficiency
HER	Hydrogen evolution reaction
ICP-OES	Inductively coupled plasma optical emission spectrometer
OCP	Open-circuit potential
RHE	Reversible hydrogen electrode
SEM	Scanning electron microscopy
SPCE	Single-pass carbon efficiency
$U_{L(CO2)}$-$U_{L(H2)}$	The limiting potential difference between CO_2RR and HER
XRD	X-ray diffraction

Italics

c	Product concentration, ppm
$E_{formate}$	Standard potential for formate production, V
ΔE	Electronic energy
FE_{HCOO-}	Faraday efficiency of formate
FE_{H2}	Faraday efficiency of H_2
$J_{formate}$	Partial current density of formate, mA cm^{-1}
Q	Total charge number, C
t	Electrolysis time, s
v	Gas flow rate, sccm
z	Electron transfer number
C_{dl}	Double layer capacitance
$E_{applied}$	Applied potential, V
F	Faraday constant, C mol^{-1}
FE_{CO}	Faraday efficiency of CO
ΔG	Gibbs free energy change, eV
n	Molar number of formate
ΔS	Entropy change
T	Temperature, K
V_m	molar volume of gas, mol L^{-1}
ΔZPE	Zero-point energy change

1. Introduction

Electrocatalytic CO_2 reduction reaction (ECO_2RR) is one of the attractive approaches for the alleviation of environmental problems arising from the continuous increase in global carbon emissions. Also, it can tackle energy shortages by converting CO_2 into value-added chemical fuels using renewable energy sources [1,2]. Formic acid and its salt (formate) are important among the products of ECO_2RR due to their economic viability and extensive applications as chemical intermediates or feedstocks [3–5]. However, the sluggish chemisorption and activation of CO_2 remain a challenge to achieving high Faraday efficiency (FE) and activity for formic acid or formate [6–8]. Main-group metal-based materials (Sn, In, Bi, Pb, etc.) are the potential catalysts for ECO_2RR to generate formate or formic acid [9–11]. SnO_2-based catalysts are especially attractive owing to their low cost, less toxicity, and suitable *OCHO adsorption strength [8]. Nevertheless, they exhibit weak adsorption and activation capacities towards CO_2, low electrical conductivity, and poor durability [12,13].

With a suitable interfacial structure, the ECO_2RR reaction rate and product selectivity can be desirably improved. It could provide a strong electronic interaction at heterointerface sites and tune the charge distribution around active sites to optimize the adsorption and desorption characteristics of reactants and key intermediates [14–16]. Furthermore, the sluggish electron transfer related to multiple proton-coupled electron transfers can be overcome with the regulation of both thermodynamic and kinetic parameters [17–19]. Recently, the construction of abundant interfacial structures by forming heterostructures between SnO_2 and other supports has become efficient in stabilizing higher oxidation states of Sn and optimizing electroactivity [10,20,21]. For instance, a 0D/2D heterojunction comprising SnO_2 nanodots confined on graphitic carbon nitride (g-C_3N_4) nanosheets was developed to expedite the conversion of CO_2 into formate. Experimental and theoretical studies showed that the robust interactions between metal oxides and supports, along with *p–p* orbitals coupling promoted the electron transfer from electron-rich g-C_3N_4, to SnO_2. Consequently, the SnO_2/g-C_3N_4 heterojunction displayed improved activity and stability for ECO_2RR to formate with a FE of 91.7% at −0.88 V *vs.* reversible hydrogen electrode (RHE) in 1.0 M KOH using a flow cell [22]. Ma et al. developed CeO_2–SnO_2 heterostructures and reported that oxygen vacancies on CeO_2 could boost the dissociation of water to generate *OH and *H species. *OH oxidized Sn^0 to form active $Sn^{\delta+}$ and facilitated the conversion of CO_2 into the key intermediate *OCHO using *H species. CeO_2–SnO_2 exhibited a maximum formate FE of 87.1% in 1 M $KHCO_3$ [20]. Unfortunately, enhancing activity and selectivity further remains a challenge due to the absence of specific regulatory principles that govern the adsorption of competing reaction intermediates. Moreover, the coupling of *p* orbitals between dual *p*-block metals has been rarely analyzed during ECO_2RR.

Herein, we report the rational construction of Bi/SnO_2 by combining wet chemistry and pyrolysis followed by a reduction step using $NaBH_4$. The strong electronic interaction by leveraging the abundant *p*-electrons of Bi makes the resulting catalysts (Bi/SnO_2) exhibit a remarkable electrocatalytic performance for ECO_2RR towards formate production with a maximum formate FE of 94.9%. The experimental and computational (density functional theory, DFT) results indicate that the coupling effect of *p–p* orbitals at the interface of Bi/SnO_2 enhances the electron transfer rates and lowers the reaction energy barrier during ECO_2RR.

2. Experimental

2.1. Chemicals

All the chemicals, including bismuth nitrate pentahydrate ($Bi(NO_3)_3{\cdot}5H_2O$, Aladdin, ≥99.99% metals basis), tin chloride dihydrate ($SnCl_2{\cdot}2H_2O$, Aladdin, 98%, AR), sodium borohydride ($NaBH_4$, Aladdin, 98%), potassium bicarbonate ($KHCO_3$, Aladdin, 99.7% dry basis), potassium hydroxide (KOH, Aladdin, AR), isopropanol (C_3H_8O, Aladdin, 99.5%, AR), bismuth (Bi, Aladdin, ≥99.999% metals basis), oxalic acid dihydrate ($C_2H_2O_4{\cdot}2H_2O$, Xilong Scientific, AR), ethanol (CH_3CH_2OH, Damao, AR), trisodium citrate dihydrate ($C_6H_5Na_3O_7{\cdot}2H_2O$, Innochem, 99%), nitric acid (HNO_3, 98wt%), and Nafion perfluorinated resin (Adamas, 5 wt.% in the mixture of lower aliphatic alcohols and water) were used directly without further purification.

2.2. Synthesis of SnO_2

0.06 mol of tin chloride dihydrate and 0.06 mol of oxalic acid dihydrate were individually dissolved in deionized water (DI water). Subsequently, the oxalic acid dihydrate solution was added to the metal salt solution while continuously stirring for one hour. Then, the obtained white precipitate was washed three times with water and ethanol. The resulting powder was subjected to drying at 80 °C for 12 h to obtain the oxalate precursor. Finally, the precursor was placed in a muffle furnace at 300 °C for one hour to obtain SnO_2.

2.3. Synthesis of Bi/SnO_2 catalysts

Initially, 0.32/0.57/0.72 mL of a 0.25 mol L^{-1} bismuth nitrate pentahydrate solution and 4 mmol trisodium citrate dehydrate were dissolved in 150 mL DI water. Meanwhile, 0.8 mL of concentrated nitric acid was added to prevent the hydrolysis of bismuth nitrate. Subsequently, 150 mg SnO_2 was uniformly dispersed in 50 mL deionized water and then added to the metal salt solution. After stirring for 20 min, 60 mL of 0.1 mol L^{-1} sodium borohydride solution was added to the above suspension. Followed by an additional 8 h of continuous stirring, the formed black precipitate was filtered and washed multiple times with DI water. Subsequently, the resultant black precipitates were subjected to vacuum drying at 60 °C to obtain Bi/SnO_2 with varying mass ratios of Bi to SnO_2, which were designated as 1:4, 1:5, and 1:9 Bi/SnO_2.

2.4. Characterization

X-ray diffraction (XRD) patterns were recorded with a Rigaku Ultima IV diffractometer with Cu Kα radiation over a range of 10–70° at a scanning rate of 4° min^{-1}. X-ray photoelectron spectroscopy (XPS) was carried out on a Kratos Analytical AXIS SUPRA spectrometer with monochromated Al K*α* radiation as an excitation source. The spectra were calibrated by referencing the C 1s peak at 284.8 eV, and measurements were conducted under an ultrahigh vacuum with charge neutralization applied. Scanning electron microscope (SEM) images were collected using a JEOL JSM7900F field-emission scanning electron microscopy. Transmission electron microscope (TEM) images were conducted with a JEOL JEM-2100 transmission electron microscope, accompanied by energy dispersive spectroscopy (EDS) analysis. An inductively coupled plasma-optical emission spectrometer (ICP-OES) was employed to determine the contents of Bi and Sn in the prepared Bi/SnO_2 catalysts. The temperature-programmed desorption of CO_2 (CO_2-TPD) was conducted on a Micromeritics AutoChem II 2920, equipped with a TCD detector. *In situ* attenuated total reflectance surface-enhanced infrared absorption spectroscopy (ATR-SEIRAS) was performed using a Bruker Tensor 27 ATR-FTIR spectrometer equipped with a liquid nitrogen-cooled MCT detector and *in situ* ATR infrared electrochemical reaction cell (EC-ATR-H) provided by Beijing Scistar Technology Co., Ltd. All spectroscopic measurements were performed at a spectral resolution of 4 cm^{-1} and overlaying of 64 repetitions. *In situ* Raman spectra were acquired using a Renishaw inVia Reflex micro-Raman spectrometer equipped with a 532 nm laser source.

2.5. Preparation of working electrodes and electrochemical measurements

Electrochemical experiments were carried out at ambient temperature using a CHI 760e workstation. Both flow-cell and H-cell configurations were employed for the three-electrode measurements. For the working electrode, 4 mg of the prepared catalyst and 1 mg of carbon black (XC-72) were dispersed into 1 mL of a mixed solution (720 μL isopropanol, 240 μL deionized water, 40 μL 0.5 wt.% Nafion solution) by sonicating for about 30 min to form a uniform ink. The catalyst ink was meticulously spread onto a hydrophobic carbon cloth with an area of 2 × 1 cm^2 to achieve the loading of 1 mg cm^{-2} as the working electrode. A Pt plate was used as the counter electrode, and an Ag/AgCl (saturated KCl) electrode was used as the reference electrode. The reference electrode was converted to RHE using the expression $E_{RHE} = E_{Ag/AgCl} + 0.197 + 0.0592 \times pH$. In a H-cell, each compartment contained about 30 mL of the electrolyte (0.5 M $KHCO_3$) with a gas headspace of 20 mL. In the flow cell system, Ar (99.99%) and CO_2 (99.99%) were supplied with a rate of 30 sccm, and the flow rate of the electrolyte (1 M KOH) was about 1.0 mL min^{-1} for both chambers. The thickness of the gaskets was about 0.5 mm. The Nafion 117 film and anion-exchange membrane (Sustanion) were used to separate the anode and cathode chambers for the H-cell and flow cell, respectively. All the potentials were compensated at 90%.

All electrochemical experiments were performed in triplicate, and the error bars were derived from these three parallel measurements to illustrate the experimental variability. The cyclic voltammetry (CV) measurements were carried out at a scan rate of 100 mV s^{-1} for 20 cycles to establish a stable CV curve before other electrochemical measurements. The linear sweep voltammetry (LSV) measurements were conducted at a scan rate of 10 mV s^{-1} to achieve a stable polarization curve. Electrochemical impedance spectroscopy (EIS) analysis was conducted at 0.05 V *vs.* RHE with a DC potential of 5 mV with frequencies ranging from 200 kHz to 0.1 Hz. The electrochemical active surface area (ECSA) of the samples in this study was determined using CV, with the potential being swept from 0.05 V above the open-circuit potential (OCP) to 0.05 V below the open-circuit potential using five different scan rates (20, 40, 60, 80, and 100 mV s^{-1}).

2.6. Analysis of electrocatalytic CO_2 reduction reaction products

A mass flow meter was provided at the outlet to measure the volume of gas leaving the system, and a gas collection bag was used to collect the gas products. The gas products were detected using an Agilent 8890 gas chromatograph (GC) equipped with a thermal conductivity detector and a flame ionization detector. After 60 min of ECO_2RR, 1.5 mL catholyte was taken out from the electrochemical cell and detected with an Agilent 1260 high-performance liquid chromatograph (HPLC). The FE of the products was calculated according to Eqs. (1) and (2).

The formate FE (FE_{HCOO-}) was calculated as below:

$$FE_{HCOO^-} = \frac{n*F*2}{Q} \quad (1)$$

where 2 is the number of transferred electrons, n is the number of moles of formate produced during the electrolysis, Q is the total charge during the electrolysis (C), and F is the Faraday constant (96,485 C mol^{-1}).

The FE for CO or H_2 (FE_{CO} or FE_{H2}) was calculated as follows:

$$FE_{H2} \text{ or } FE_{CO} = \frac{c*v*F*z}{10^6*Q*V_m} \quad (2)$$

where c is the concentration of CO or H_2 listed by GC, v is the CO_2 flow rate, z is the number of transferred electrons, and for H_2 and CO, the z is

2, F is the Faraday constant (96,485 C mol^{-1}), Q is the total charge during the electrolysis (C), and V_m is the molar volume of the gas products at the laboratory temperature (24.5 mol L^{-1}). International units are utilized in this work.

The single pass carbon efficiency (SPCE) was calculated as follows.

$$SPCE = \frac{(J \times t)/(2 \times F)}{(v \times t)/V_m} \times 100\% \quad (3)$$

where J is the partial current density of formate/formic acid, 2 is the number of electrons transferred from CO_2 to formate/formic acid, F is the Faraday constant (96,485 C mol^{-1}), and v is the flow rate of CO_2, t is the electrolysis time (30 min), V_m is the molar volume of the gas products at the laboratory temperature (24.5 mol L^{-1}).

The half-cell energy efficiency (cathodic energy efficiency, CEE) was calculated as follows:

$$CEE = \frac{1.23 - E_{formate}}{1.23 - E_{applied}} \times FE_{formate} \times 100\% \quad (4)$$

where $E_{formate}$ is the standard potential for formate production (−0.2 V *vs.* RHE), $E_{applied}$ is the applied potential *vs.* RHE in the flow cell, and $FE_{formate}$ is the FE of formate.

2.7. Density functional theory calculations

DFT calculations were carried out employing the Vienna Ab initio simulation package (VASP). The exchange–correlation potential was described using the generalized gradient approximation of the revised Perdew-Burke-Ernzerhof functional. The interactions between ion cores and valence electrons were treated using the projector-augmented waves (PAW) method, with a cutoff energy of 450 eV applied for plane waves. To simulate the catalyst structure in the experiment, the Bi (012) and SnO_2 (110) surfaces were employed to establish the respective computational models for Bi and SnO_2. A three-layer simulation framework was applied to both materials. Additionally, the three-layer Bi slab and the three-layer SnO_2 slab were aligned laterally to form a reasonable Bi/SnO_2 heterostructure. An 11 Å vacuum layer was introduced along the z-axis to prevent interactions between the slab and its periodic images. The Monkhorst-Pack method was employed for sampling the Brillouin zone. A (2 × 2 × 1) k-point grid was used for optimizing the supercell structures of Bi and SnO_2, whereas a (2 × 1 × 1) k-point grid was applied for the Bi/SnO_2 supercell structure optimization. For the density of states calculations, a (4 × 4 × 1) k-point grid was utilized. The bottom layer of the structures was constrained, while the other layers were allowed to relax. The structural models underwent relaxation until the Hellmann-Feynman forces became smaller than −0.02 eV/Å while ensuring that the change in energy remained below 10^{-5} eV. For the optimized structures, vibrational frequencies were calculated to determine zero-point energies, thermal corrections, and entropy contributions. Furthermore, a convergence tolerance of 10^{-6} eV was established with relaxation only permitted for the adsorbed species during the calculation of vibrational frequencies.

The definition of the Gibbs free energy change is,

$$\Delta G = \Delta E + \Delta ZPE - T\Delta S$$

where ΔE signifies the electronic energy calculated using VASP, ΔZPE is the zero-point energy difference, ΔS is the entropy change between the reactants and products, and T denotes the fixed temperature (298.15 K).

The limiting potential difference between CO_2RR and HER ($U_{L(CO2)}$-$U_{L(H2)}$) is,

$$U_{L(CO2)} - U_{L(H2)} = -\frac{\Delta G_{RDS,H2} - \Delta G_{RDS,CO2}}{e} \quad (5)$$

where $U_{L(CO2)}$ and $U_{L(H2)}$ represent the limiting potentials of the CO_2RR and HER reactions, $\Delta G_{RDS,H2}$ and $\Delta G_{RDS,CO2}$ represent the maximum free energy change corresponding to the rate-determining step (RDS) in the reaction pathways of HER and CO_2RR, respectively, and e represents the electric charge of a single electron.

3. Results and discussion

3.1. Synthesis and characterization of Bi/SnO_2

The schematic showing the synthesis of heterostructure Bi/SnO_2 is depicted in Fig. 1a. SnO_2 nanosheets were initially synthesized by calcining a single-phase tin oxalate (Fig. S1 in the supporting information (**SI**)) under an air atmosphere [21]. Subsequently, Bi nanoparticles were loaded onto the SnO_2 nanosheets through impregnation followed by reduction using $NaBH_4$. In this study, Bi/SnO_2 heterostructures with varying mass ratios of Bi to SnO_2 (1:4, 1:5, and 1:9) were systematically prepared and designated as 1:4 Bi/SnO_2, 1:5 Bi/SnO_2, and 1:9 Bi/SnO_2 (Fig. S2 of **SI**). The crystal structure of Bi/SnO_2 was further investigated using XRD. As illustrated in Fig. 1b, the diffraction peaks corresponding to SnO_2 are indexed to the rutile phase. A weak diffraction peak noticed at 27.06° associated with Bi nanoparticles was observed in the XRD pattern of Bi/SnO_2. It confirms the incorporation of Bi nanoparticles into the composite material. The mass fractions of Bi and Sn in the Bi/SnO_2 catalyst, as determined by ICP-OES, exhibit a general concordance with the theoretical contents (Table S1 of **SI**). The SEM images reveal that SnO_2 nanosheets possess a relatively smooth surface and exhibit a uniform distribution in various orientations (Fig. S3 of **SI**). Fig. 1c clearly shows that the prepared Bi/SnO_2 composites exhibit a sheet morphology similar to that of SnO_2, but with a rough surface layer, which further confirms the loading of Bi nanoparticles. Moreover, the SEM images (Figs. S4–S6 of **SI**) reveal that the agglomeration of Bi nanoparticles is more apparent with the increase of Bi content. Fig. S6 of **SI** shows the uniform dispersion of Bi nanoparticles over SnO_2 nanosheets. TEM images in Fig. S7 of **SI** show the typical lamellar morphology for heterostructure 1:5 Bi/SnO_2. The high-resolution TEM (HRTEM) images (Fig. 1d) display two evident lattice fringes of 0.394 and 0.269 nm corresponding to the Bi (003) plane and SnO_2 (1 0 1) plane, respectively [23,24]. Intriguingly, the heterostructure Bi/SnO_2 exhibits the multiple interfaces between Bi and SnO_2 nanocrystals, as illustrated in Fig. 1e. It corroborates the formation of heterostructures between SnO_2 and Bi. EDS elemental mapping images of Bi/SnO_2 (Fig. 1f) indicate the uniform distribution of Sn and Bi elements throughout the catalyst.

The chemical composition and oxidation state of the synthesized electrocatalysts were systematically characterized using XPS in Fig. S8 of **SI.** As shown in Fig. 2, the binding energy values of Bi and Sn in Bi/SnO_2 present positive and negative shifts, respectively, compared to that of pure Bi and SnO_2, indicating the electron transfer from Bi to Sn. In Fig. 2a, the peaks noticed at 486.7 eV and 495.2 eV are assigned to Sn^{4+} of SnO_2. In the high-resolution Bi 4*f* spectra (Fig. 2b), the peaks located at 156.6 eV and 161.9 eV are ascribed to the metallic Bi and the other two peaks at 158.7 eV and 164.0 eV are contributed to Bi^{3+} owing to the oxidation by exposing the samples in the air [25]. The binding energies of Sn $3d_{5/2}$ and Sn $3d_{3/2}$ are shifted to lower energies with decreasing amounts of Bi, as shown in Fig. S9 of **SI**. On the other hand, as the amount of Bi decreases, the Bi^0 $4f_{7/2}$ and Bi^0 $4f_{5/2}$ peaks are shifted to larger binding energies. These findings provide unequivocal evidence that electrons are transferred from Bi to SnO_2, thereby modifying the overall electronic structure of the active sites at the Bi/SnO_2 interface [26]. The electronic interactions at the interface of Bi and SnO_2 offer a promising prospect for regulating electrocatalytic properties. Furthermore, Ar^+ etching was utilized to substantiate the existence of metallic Bi in the bulk phase of Bi/SnO_2 (Fig. S10). Meanwhile, the chemical state of pure Bi before and after Ar^+ etching was also investigated as a reference. Fig. S10 of **SI** demonstrates that the peak intensity of Bi^0 increases with the extension of Ar^+ etching time for both pure Bi and Bi/SnO_2, indicating the oxidation of surface metallic Bi in air [27].

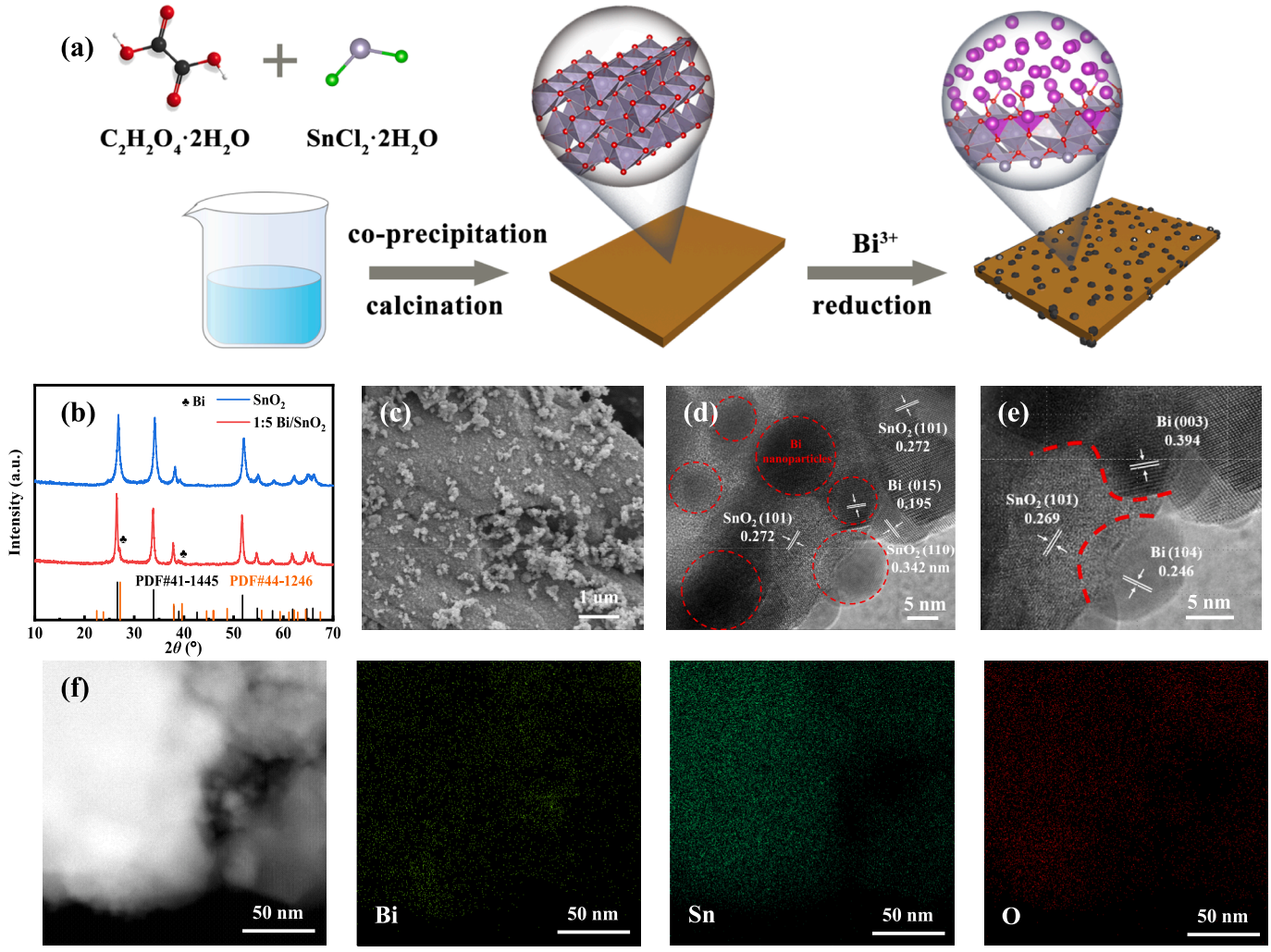

Fig. 1. (a) Schematic showing the synthesis of Bi/SnO_2; (b) XRD patterns of Bi, SnO_2 and Bi/SnO_2 nanosheets; (c) SEM image of 1:5 Bi/SnO_2 nanosheets; (d-e) HRTEM images of 1:5 Bi/SnO_2 nanosheets where some Bi nanoparticles and heterogeneous interfaces were marked with red dashed lines; (f) Elemental mapping images of 1:5 Bi/SnO_2 nanosheets. (For interpretation of the references to colour in this figure legend, the reader is referred to the web version of this article.)

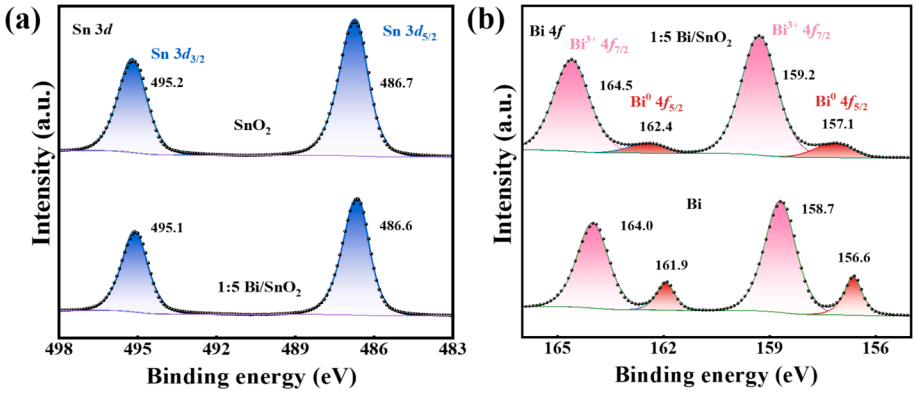

Fig. 2. High-resolution (a) Sn 3*d* and (b) Bi 4*f* XPS spectra for 1:5 Bi/SnO_2.

3.2. *Electrochemical CO_2 reduction reaction activity evaluation*

The ECO_2RR performances of the prepared catalysts were initially evaluated in a gas-tight two-compartment H-cell with the three-electrode system in 0.5 M $KHCO_3$. Fig. 3a shows LSV curves of pure Bi, SnO_2, and 1:5 Bi/SnO_2 catalysts. The current densities of the three catalysts at the same applied potential in CO_2-saturated electrolyte are significantly higher than those in Ar-saturated electrolyte, indicating their favorable ECO_2RR activity. Among them, Bi/SnO_2 exhibits the highest current density, revealing its best ECO_2RR performance. The gaseous products from ECO_2RR were quantified by GC, and liquid products were analyzed by HPLC (Fig. S11 of **SI**), respectively. Only

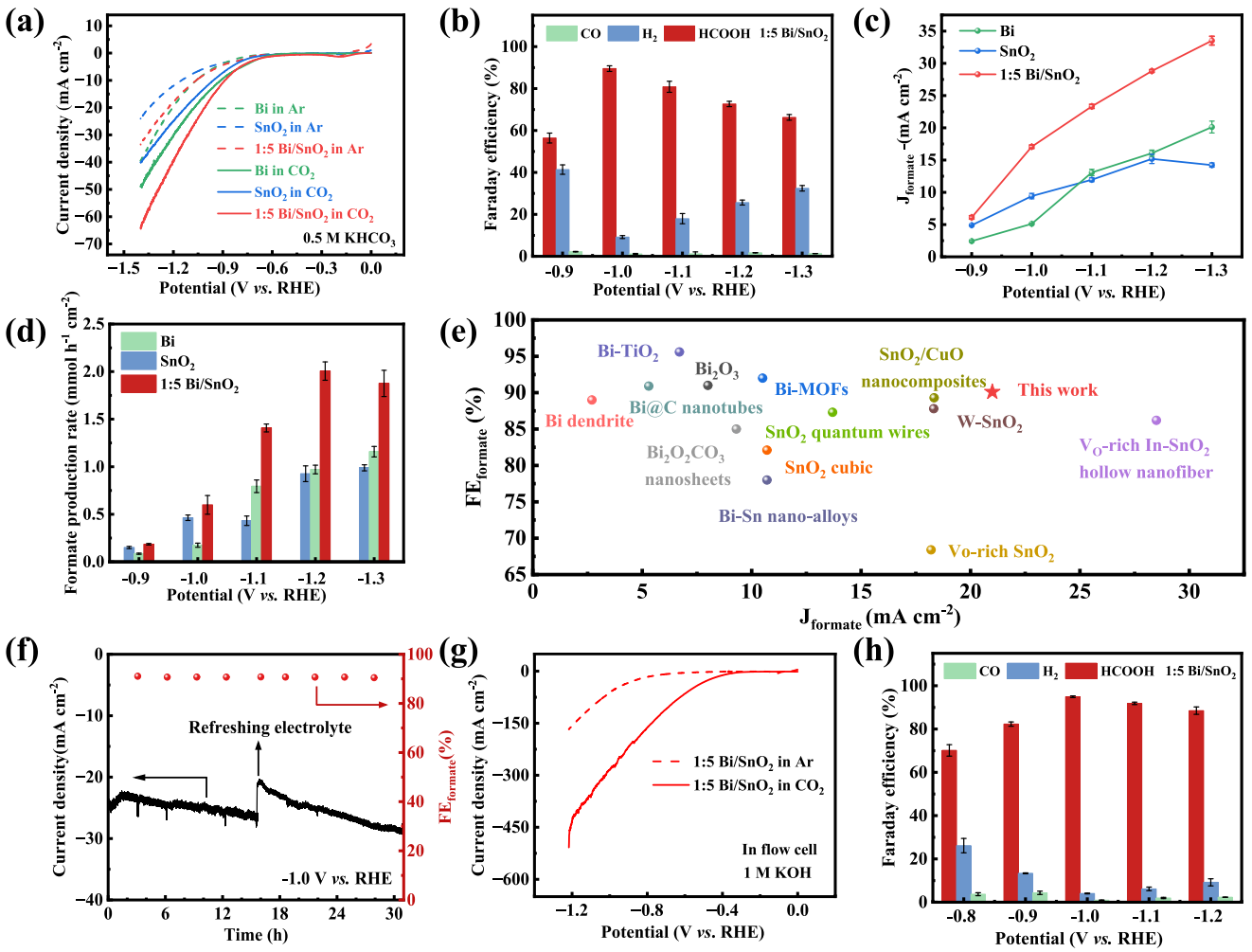

Fig. 3. ECO_2RR measurements: (a) LSV curves of Bi, SnO_2 and 1:5 Bi/SnO_2 tested in Ar and CO_2-saturated 0.5 M $KHCO_3$ aqueous solution in H-cell, respectively; (b) $FE_{formate}$ for 1:5 Bi/SnO_2; (c) $J_{formate}$ under different applied potentials for Bi, SnO_2 and 1:5 Bi/SnO_2; (d) Formate production rate of Bi, SnO_2 and 1:5 Bi/SnO_2; (e) Comparison of formate selectivity at optimum potential for Bi/SnO_2 nanosheets with reported Sn-based catalysts; (f) Stability test over 1:5 Bi/SnO_2 catalyst measured in 0.5 M $KHCO_3$ at −1.0 V *vs.* RHE; (g) LSV curve of 1:5 Bi/SnO_2 in flow cell saturated with 1 M KOH in Ar and CO_2; (h) Faraday efficiency of reduction products at each applied potential for 1:5 Bi/SnO_2 in flow-cell; The error bar represents the standard deviation of at least three independent measurements, indicating that the data are variable.

formate, H_2, and CO were detected in this work (Fig. 3b). The maximum $FE_{formate}$ for Bi/SnO_2 is 90.5% at −1.0 V *vs.* RHE, surpassing that of SnO_2 (61.7%) and pure Bi (41.9%), as given in Fig. S12 of **SI**. Additionally, the electrocatalytic performance of samples with varying mass ratios of Bi to SnO_2 (1:4 Bi/SnO_2 and 1:9 Bi/SnO_2) was also measured (Figs. S13–14 of **SI**) to explore the effect of catalyst composition on the selectivity of CO_2 reduction, and 1:5 Bi/SnO_2 exhibits the best activity. This result may be benefited from the modest Bi-O-Sn interface of 1:5 Bi/SnO_2. Then, the formate partial current density ($J_{formate}$) and formate production rate were used to compare their ECO_2RR performance. It is noteworthy that 1:5 Bi/SnO_2 catalysts present a $J_{formate}$ of 28.8 mA cm^{-2} at −1.2 V with a formate production rate, significantly superior to that of SnO_2 (15.2 mA cm^{-2}) and pure Bi (16.1 mA cm^{-2}) (Fig. 3c and d). Notably, the ECO_2RR performance of 1:5 Bi/SnO_2 is better than most of the recently reported Sn-based catalysts (Fig. 3e and Table S2 of **SI**). The stability of the Bi/SnO_2 catalysts for ECO_2RR was assessed through chronoamperometry at −1.0 V *vs.* RHE. As shown in Fig. 3f, the current density and $FE_{formate}$ only exhibit small fluctuations due to the accumulation of formate concentration over 30 h of electrolysis. An average current density of 25 mA cm^{-2} and the $FE_{formate}$ are kept around 90% during the entire stability test. This indicates the desirable stability of Bi/SnO_2. Post-reaction XRD analysis of SnO_2 catalysts and Bi/SnO_2 catalysts (Fig. S14 of **SI**) reveals that SnO_2 is inevitably partially converted to metallic Sn during the ECO_2RR process under relatively negative potential [28]. To investigate the impact of the metallic Sn on the ECO_2RR, pre-reduction experiments were performed on the SnO_2 catalyst at a potential of −1.0 V *vs.* RHE. The LSV curves shown in Fig. S15 of **SI** demonstrate that the catalytic activity significantly declines after the partial reduction of SnO_2 to Sn. This phenomenon can be ascribed to the disruption of the oxide layer on the surface of the SnO_2 electrode, in line with earlier reports [29].

To evaluate the practical values under industrial–scale current densities exceeding 100 mA cm^{-2}, the catalysts were assembled in the flow cell. The electrochemical performance of the 1:5 Bi/SnO_2 catalyst was evaluated in 1 M KOH electrolyte (Fig. 3g). The $FE_{formate}$ reaches 94.9% at −1.0 V *vs.* RHE with a yield of up to 3.05 mmol h^{-1} cm^{-2} (Fig. S16 of **SI**). It shows that the FE and yield of formate in the flow cell are increased, i.e., approximately a 5.8 times increase of formate yield increase, as compared to the H-cell. Furthermore, the average selectivity for formate is more than 90% at an average current density of 300–500 mA cm^{-2} of formate in 1 M KOH, as shown in Fig. 3h. This indicates the significant industrial values of Bi/SnO_2. The cathodic energy efficiency (CEE) and the single-pass carbon efficiency (SPCE) are defined as the ratio of chemical energy stored in the target product to the electrical

energy input and the molar ratio of CO_2 converted to product formate to the molar input of CO_2 fed into the reactor. They are crucial parameters for the practical application of ECO_2RR. The CEE can reach 60.9% at −1.0 V *vs.* RHE. Plots of FE and SPCE over the CO_2 gas flow rate are depicted in Fig. S17 of **SI**. The SPCE of the Bi/SnO_2 catalyst can attain a value of 40.3% at a potential of −1.0 V *vs.* RHE when the CO_2 flow rate is reduced from 30 to 3 standard cubic centimeters per minute (sccm) in the flow cell, meanwhile, the $FE_{formate}$ is still maintained at a high level. Therefore, the Bi/SnO_2 catalyst is capable of effectively harnessing a considerable amount of electrical energy for formate production throughout the reaction.

3.3. Origin of CO_2 reduction performance of Bi/SnO_2

To explore the origin of the improved ECO_2RR performance of Bi/SnO_2, the factors including the ECSA, charge transfer capacity, CO_2 adsorption capacity, and dynamic evolution of the catalysts and reaction intermediates were comprehensively examined. ECSA was estimated by calculating the double-layer capacitance (C_{dl}). The C_{dl} value was determined via CV measurements performed in Ar-saturated electrolytes across a range of scan rates (Fig. S18 of **SI**). Fig. 4a indicates a negligible difference in C_{dl} between the three catalysts corresponding to the almost similar ECSA value (Table S3 of **SI**), indicating that Bi/SnO_2 is intrinsically more active than pure Bi and SnO_2 [30]. Subsequently, EIS measurements were performed to evaluate the charge transfer behavior [31,32]. The Nyquist plots depicted in Figs. 4b and S19 of **SI** reveal that the Bi/SnO_2 demonstrates a markedly lower charge transfer resistance compared to pure SnO_2 and Bi. This improvement can be attributed to the enhanced electron transfer facilitated by the formation of the Bi-O-Sn interface within Bi/SnO_2. Meanwhile, the CO_2 adsorption capacity of Bi/SnO_2 was investigated by CO_2-TPD measurements (Fig. 4c). It shows that the loading of Bi metal on the SnO_2 surface increases the area of the desorption peak observed between 300 and 320 °C due to adsorption of CO_2 preferentially on the surface of Bi/SnO_2. A reduced Tafel slope value generally indicates relatively a rapid increase in current density with increasing overpotential, suggesting superior catalytic performance of the catalyst. Therefore, the Tafel slope of Bi/SnO_2 (64 mV dec^{-1}) lower than that of pure Bi (114 mV dec^{-1}) and SnO_2 (115 mV dec^{-1}) demonstrates its best performance for ECO_2RR (Fig. 4d), which is in line with the performance evaluation [33]. Furthermore, a quasi-first-order dependency (0.88, Fig. 4e) of the formate partial current density on bicarbonate concentration over Bi/SnO_2 is obtained, implying the participation of HCO_3^- in the formate formation [11].

To track the evolution of reaction intermediates during ECO_2RR by Bi/SnO_2, *in situ* ATR-SEIRAS (Fig. 4f) and in situ Raman spectroscopy (Fig. S20 of **SI**) were conducted. The *in-situ* ATR–SEIRAS spectra of Bi/SnO_2 under CO_2 atmosphere within the potential range spanning from −0.6 to −1.4 V *vs.* RHE exhibit several distinct infrared bands. The Bi/SnO_2 catalyst exhibits characteristic peaks at 1269, 1380, 1520, 1650 and 3000–3600 cm^{-1} at various operating potentials, which are

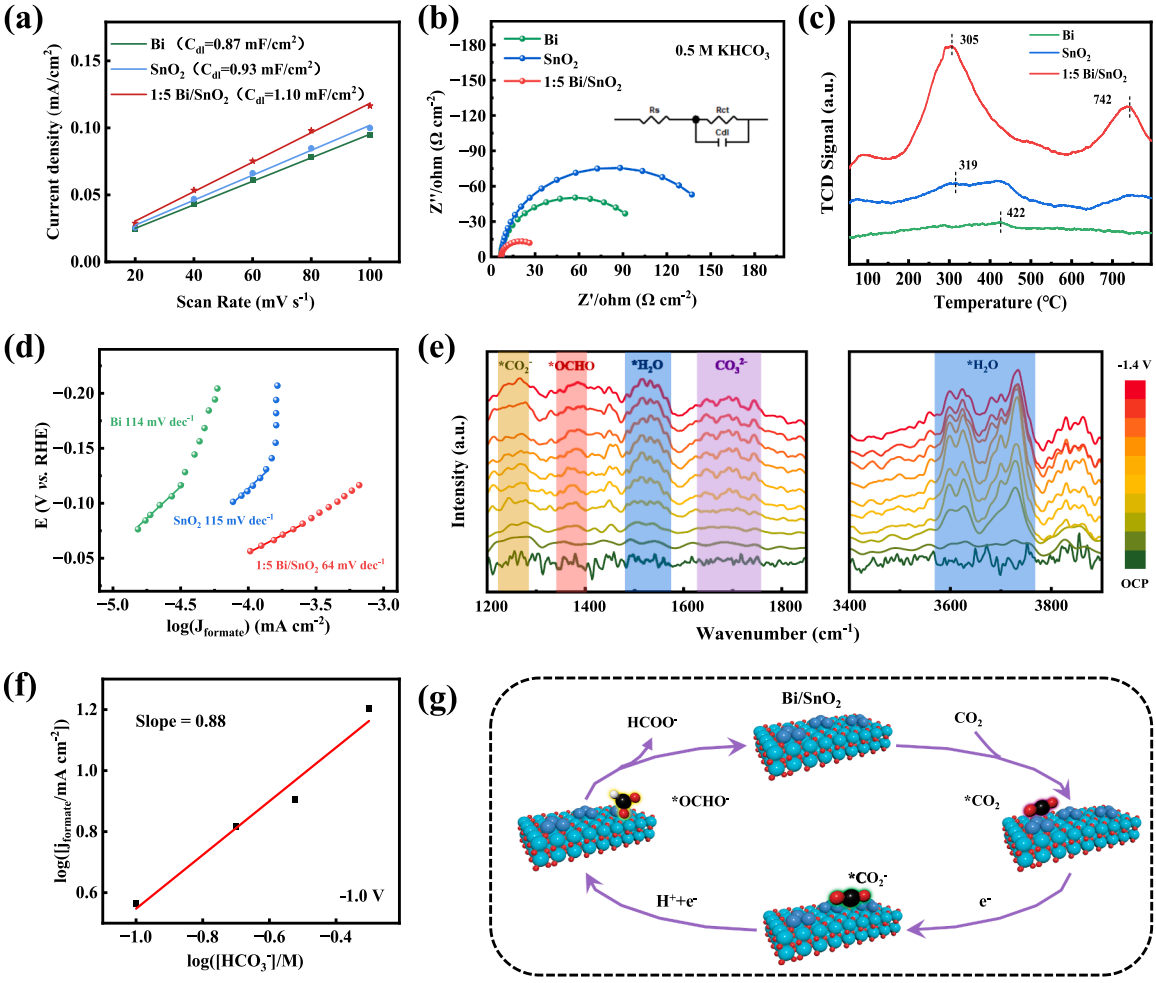

Fig. 4. Studies on ECO_2RR catalytic mechanism: (a) plots of current density at various scan rates; (b) EIS curves and equivalent circuit (inset) recorded at −1.0 V *vs.* RHE; (c) CO_2-TPD curves for Bi, SnO_2 and 1:5 Bi/SnO_2; (d) Tafel plots of formate product of the Bi, SnO_2 and 1:5 Bi/SnO_2; (e) *In situ* ATR-FTIR of 1:5 Bi/SnO_2 in CO_2-saturated 0.5 M $KHCO_3$ between −0.6 V and −1.4 V *vs.* RHE; (f) Rate dependency on the concentration of bicarbonate ($[HCO_3^-]$) for 1:5 Bi/SnO_2 at −1.0 V *vs.* RHE; (g) Schematic representation of the CO_2RR pathway for formate.

attributed to the C=O vibration of $*CO_2^-$ [34], the O–C–O vibration of *OCHO [11], H–O–H bending vibration of H_2O [35], the vibration of CO_3^{2-}, and O–H stretching vibration of H_2O [34,36], respectively. With the increase of applied potential, the intensity of the *OCHO band gets strengthened and indicates the formation of formate through the *OCHO pathway. Concurrently, the characteristic peaks of $*CO_2^-$ and CO_3^{2-} exhibit a gradual increase with programmed applied negative potential due to the gradual extending of the reaction during the ECO_2RR. Furthermore, the increase of CO_3^{2-} band intensity implies the continuous consumption of HCO_3^- as a proton source. In addition, the increase in the intensity of the O–H stretching band of H_2O from −0.6 to −1.4 V *vs.* RHE indicates that Bi/SnO_2 surface enriches more interfacial H_2O molecules and the proton source during CO_2 reduction is not H_2O. *In situ* Raman spectroscopy measurements reveal that the characteristic peaks at 490 cm^{-1} and 606 cm^{-1} (Fig. S19 of **SI**) correspond to the E_g and A_{1g} vibrations of Sn-O bonds in SnO_2, respectively [29,37]. With the increase of applied voltage, these peak maintain their intensities, which suggests that the surface of Bi/SnO_2 catalyst exhibits a relatively robust structure. The distinctive peaks observed at 1060–1070 cm^{-1} and 1530–1580 cm^{-1} are attributed to the symmetric C–O stretching vibration of $CO_3^{2-}$and the asymmetric O–C–O stretching vibration of *OCHO, respectively [10,38]. With the increase of applied potential from −0.8 to −1.2 V *vs.* RHE, the intensity of the peak at 1060–1070 cm^{-1} exhibits a gradual increase, which indicates the increased CO_3^{2-} concentration. In combination with the results showin in Fig. 4f, these observations incdicate the participation of H^+ from HCO_3^- in the reaction. In addition, the peak at 1530–1580 cm^{-1} displays a declining trend due to the continuous consumption of *OCHO intermediates with the increase of applied potential after stopping the CO_2 bubbling into the CO_2-saturated electrolyte. Based on the above-mentioned results, the plausible ECO_2RR mechanism is proposed in Fig. 4g.

3.4. Enhanced intrinsic activity mechanism by the DFT calculations

To achieve a comprehensive understanding of the mechanisms underlying the enhanced intrinsic activity, the DFT calculations were employed and the variations in electronic properties and Gibbs free energy change were analyzed. Bi (012), SnO_2 (110), and Bi/SnO_2 were constructed and optimized (Fig. S21 of **SI**) based on XRD and HRTEM results (Fig. 1b, d–e). The electronic properties of interfacial catalyst Bi/SnO_2 were investigated by differential charge density distribution and projected density of states (PDOS). The differential charge density distribution of the Bi/SnO_2 heterostructure, as shown in Fig. 5a, reveals that electrons are transferred from Bi to the SnO_2 layer, in alignment with XPS results (Fig. 2a and b) [39]. This validates the existence of a significant electronic interaction between Bi and SnO_2, which promotes charge transfer in ECO_2RR [20]. According to PDOS of *p*-orbitals of Bi atoms (Fig. 5b), and Sn and O atoms (Fig. 5c), the *p*-orbitals of Bi atoms couple with those of Sn and O atoms in the Bi/SnO_2 heterostructure. On one hand, this *p-p* orbital coupling facilitates electron transfer from Bi to SnO_2, leading to the peaks of Sn and O near the Fermi level (E_f) crossing over the Fermi level, which endows the system with metallic characteristics and significantly enhances conductivity. It is corroborated by EIS data which validates further the role of Bi in modulating the conductive properties of SnO_2. On the other hand, the *p-p* orbital coupling shifts the *p*-band center (ε_p) of Bi towards the Fermi level, thereby effectively modulating and optimizing the adsorption strength of intermediates [40,41]. Furthermore, the same is also supported by the variations in Gibbs free energy during the ECO_2RR on Bi, SnO_2, and the Bi/SnO_2 heterostructure. Different reaction routes towards formate (Fig. 5d), CO (Fig. 5e), and H_2 (Fig. S21 of **SI**) during the ECO_2RR process were considered and adsorption configurations of reaction intermediates on different catalysts were optimized and presented in Figs. S22–S23 of **SI**. To evaluate the selectivity for different products, the rate-determining step (RDS) of the reaction is determined by the Gibbs free energy change on the catalyst surface [20]. The RDS for CO_2 conversion to formate is marked by the formation of the *OCHO intermediate, while the RDS for CO_2 conversion to CO involves the formation of the *COOH intermediate. As shown in Fig. 5d and e, the RDS for the pathway of CO_2 conversion to formate is significantly lower than that for CO_2 conversion to CO, suggesting that the ECO_2RR to formate is the preferrable pathway [40,41]. When formate is the target product, the RDS for Bi, SnO_2, and Bi/SnO_2 heterostructures is associated with the formation of the *OCHO intermediate, and their Gibbs free energy change follows the order of Bi/SnO_2 (0.26 eV) < SnO_2 (0.54 eV) < Bi (0.78 eV). This suggests that the Bi/SnO_2 heterostructure could energetically facilitate the ECO_2RR into formate. Furthermore, the hydrogen evolution reaction (HER) dominates the competing reaction during ECO_2RR. The limiting potential difference between CO_2RR and HER ($U_{L(CO2)}$-$U_{L(H2)}$) was used to predict the selectivity of ECO_2RR, and a more positive value denotes a higher selectivity towards ECO_2RR [42,43]. As shown in Fig. 5f, the $U_{L(CO2)}$-$U_{L(H2)}$ value on Bi/SnO_2 is 1.09 V, which is much more positive than those on Bi (−0.25 V) and SnO_2 (0.68 V). This result suggests that ECO_2RR is preferable on Bi/SnO_2, in accordance

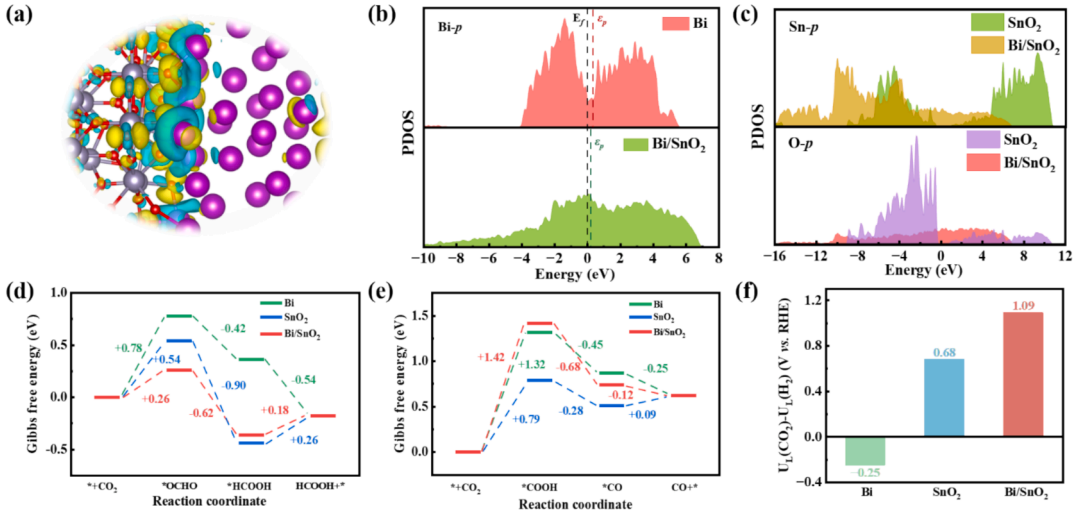

Fig. 5. (a) Differential charge density of Bi/SnO_2 (yellow display electron accumulation, cyan indicate electron depletion); (b) The DOS of Bi atoms of metal Bi and Bi/SnO_2; (c) The DOS of Sn and O atoms of Bi/SnO_2. Calculated reaction energy profiles for (d) HCOOH and (e) CO formation on pure Bi, SnO_2, and Bi/SnO_2; (f) The values of $U_{L(CO2)}$-$U_{L(H2)}$ for Bi, SnO_2, and Bi/SnO_2 catalysts. (For interpretation of the references to colour in this figure legend, the reader is referred to the web version of this article.)

with electrochemical performance data presented in Fig. 3b.

4. Conclusions

In summary, a Bi/SnO_2 heterostructure electrocatalyst has been constructed through wet chemical synthesis and pyrolysis for CO_2 reduction to formate. The underlying mechanism has been elucidated to show how interfacial engineering enhances the electrocatalytic reduction of CO_2 to formate. In a flow cell, the 1:5 Bi/SnO_2 catalyst has achieved a $FE_{formate}$ of 94.9% and a current density of 300 mA cm^{-2} at −1.0 V (*vs.* RHE) than most reporte literatures [7,8,32]. The Bi-O-Sn interfacial structure is crucial in enhancing the catalytic performance by promoting electron transfer and enhancing the adsorption and activation of CO_2. The *p-p* orbital coupling at the Bi/SnO_2 interface induces directional electron transfer from Bi to SnO_2 and thereby optimizes the adsorption strength of the *OCHO intermediate, according to computational insights. The theoretical and experimental results conclude that the *p-p* orbital coupling at dual p-block metal interfaces serves as the key parameter for the formate generation. Thus, this work provides a novel strategy for designing high-performance CO_2 reduction catalysts through interfacial engineering and electronic structure modulation.

CRediT authorship contribution statement

Zeyu Wang: Methodology, Investigation, Formal analysis, Data curation. **Yaling Jia:** Writing – original draft, Validation, Methodology, Conceptualization. **Shangqing Zhao:** Validation, Formal analysis. **Huiling Zheng:** Validation. **Antony Rajendran:** Project administration. **Wen-Ying Li:** Writing – review & editing, Supervision, Resources, Project administration, Conceptualization.

Declaration of competing interest

The authors declare that they have no known competing financial interests or personal relationships that could have appeared to influence the work reported in this paper.

Acknowledgments

The authors are greatly thankful for financial support from the National Key Research and Development Program of China (2022YFE0208400), the Fundamental Research Project of Shanxi Province (202303021212031), and the Fundamental Research Funds for the Central Universities (2022ZFJH004).

Appendix A. Supplementary data

Figs. S1–S23 and Tables S1–S3 are described in the text, please refer to the supporting materials. Supplementary data to this article can be found online at https://doi.org/10.1016/j.jcis.2025.137528.

Data availability

The data that support the findings of this study are available from the corresponding authors upon reasonable request.

References

[1] W. Yang, Q. Mo, Q.-T. He, X.-P. Li, Z. Xue, Y.-L. Lu, J. Chen, K. Zheng, Y. Fan, G. Li, C.-Y. Su, Anion modulation of Ag-imidazole cuboctahedral cage microenvironments for efficient electrocatalytic CO_2 reduction, Angew. Chem. Int. Ed. 63 (2024) e202406564.
[2] Y.-Y. Liu, J.-R. Huang, H.-L. Zhu, P.-Q. Liao, X.-M. Chen, Simultaneous capture of CO_2 boosting its electroreduction in the micropores of a metal–organic framework, Angew. Chem. Int. Ed. 62 (2023) e202311265.
[3] N. Han, P. Ding, L. He, Y. Li, Y. Li, Promises of main group metal-based nanostructured materials for electrochemical CO_2 reduction to formate, Adv. Energy Mater. 10 (2020) 1902338.
[4] J.X. Zhu, J.T. Li, R.H. Lu, R.H. Yu, S.Y. Zhao, C.B. Li, L. Lv, L.X. Xia, X.B. Chen, W. W. Cai, J.S. Meng, W. Zhang, X.L. Pan, X.F. Hong, Y.H. Dai, Y. Mao, J. Li, L. Zhou, G.J. He, Q.Q. Pang, Y. Zhao, C. Xia, Z.Y. Wang, L.M. Dai, L.Q. Mai, Surface passivation for highly active, selective, stable, and scalable CO_2 electroreduction, Nat. Commun. 14 (2023) 4670.
[5] J. Bok, S.Y. Lee, B.-H. Lee, C. Kim, D.L.T. Nguyen, J.W. Kim, E. Jung, C.W. Lee, Y. Jung, H.S. Lee, J. Kim, K. Lee, W. Ko, Y.S. Kim, S.-P. Cho, J.S. Yoo, T. Hyeon, Y. J. Hwang, Designing atomically dispersed Au on tensile-strained Pd for efficient CO_2 electroreduction to formate, J. Am. Chem. Soc. 143 (2021) 5386–5395.
[6] C. Wang, Z. Lv, Y. Liu, R. Liu, C. Sun, J. Wang, L. Li, X. Liu, X. Feng, W. Yang, B. Wang, Hydrogen-bonded organic framework supporting atomic Bi-N_2O_2 sites for high-efficiency electrocatalytic CO_2 reduction, Angew. Chem. Int. Ed. 63 (2024) e202404015.
[7] C. Hu, L. Zhang, L. Li, W. Zhu, W. Deng, H. Dong, Z.-J. Zhao, J. Gong, Theory assisted design of N-doped tin oxides for enhanced electrochemical CO_2 activation and reduction, Sci. China Chem. 62 (2019) 1030–1036.
[8] J. Chen, B. Ma, Z. Xie, W. Li, Y. Yang, M. Mu, X. Zou, B. Zhao, W. Song, Bifunctional porous SnO_2/Ag nanofibers for efficient electroreduction of carbon dioxide to formate and its mechanism elucidation by in-situ surface-enhanced Raman scattering, Appl. Catal. B Environ. 325 (2023) 122350.
[9] X. Zhong, T. Yang, S. Liang, Z. Zhong, H. Deng, Boron dopant modulated electron localization of tin oxide for efficient electrochemical CO_2 reduction to formate, Small 19 (2023) 2303185.
[10] B. Ren, G. Wen, R. Gao, D. Luo, Z. Zhang, W. Qiu, Q. Ma, X. Wang, Y. Cui, L. Ricardez-Sandoval, A. Yu, Z. Chen, Nano-crumples induced Sn-Bi bimetallic interface pattern with moderate electron bank for highly efficient CO_2 electroreduction, Nat. Commun. 13 (2022) 2486.
[11] X. Cao, Y. Tian, J. Ma, W. Guo, W. Cai, J. Zhang, Strong p-d orbital hybridization on bismuth nanosheets for high performing CO_2 electroreduction, Adv. Mater. 36 (2023) e2309648.
[12] Y. Jiang, J. Shan, P. Wang, L. Huang, Y. Zheng, S.-Z. Qiao, Stabilizing oxidation state of SnO_2 for highly selective CO_2 electroreduction to formate at large current densities, ACS Catal. 13 (2023) 3101–3108.
[13] H. Liu, B. Li, Z. Liu, Z. Liang, H. Chuai, H. Wang, S.N. Lou, Y. Su, S. Zhang, X. Ma, Ceria-mediated dynamic $Sn^0/Sn^{\delta+}$ redox cycle for CO_2 electroreduction, ACS Catal. 13 (2023) 5033–5042.
[14] T.-J. Wang, L.-B. Sun, X. Ai, P. Chen, Y. Chen, X. Wang, Boosting formate electrooxidation by heterostructured PtPd alloy and oxides nanowires, Adv. Mater. 36 (2024) 2403664.
[15] L. Fu, Z. Qu, L. Zhou, Y. Ding, Boosting electrochemical CO_2 reduction to CO over interfacial hydroxide-metal catalysts, Appl. Catal. B Environ. 339 (2023) 123170.
[16] C. Ren, S. Lu, Y. Wu, Y. Ouyang, Y. Zhang, Q. Li, C. Ling, J. Wang, A universal descriptor for complicated interfacial effects on electrochemical reduction reactions, J. Am. Chem. Soc. 144 (2022) 12874–12883.
[17] X. Zhao, Q. Feng, M. Liu, Y. Wang, W. Liu, D. Deng, J. Jiang, X. Zheng, L. Zhan, J. Wang, H. Zheng, Y. Bai, Y. Chen, X. Xiong, Y. Lei, Built-in electric field promotes interfacial adsorption and activation of CO_2 for C_1 products over a wide potential window, ACS Nano 18 (2024) 9678–9687.
[18] L. Lv, X. He, J. Wang, Y. Ruan, S. Ouyang, H. Yuan, T. Zhang, Charge localization to optimize reactant adsorption on KCu_7S_4/CuO interfacial structure toward selective CO_2 electroreduction, Appl. Catal. B Environ. 298 (2021) 120531.
[19] H. Li, H. Huang, W. Huang, X. Zhang, G. Hai, F. Lai, T. Zhu, S. Bai, N. Zhang, T. Liu, Interfacial accumulation and stability enhancement effects triggered by built-in electric field of SnO_2/LaOCl nanofibers boost carbon dioxide electroreduction, Small 20 (2024) 2402654.
[20] X. Ren, F. Liu, H. Wu, Q. Lu, J. Zhao, Y. Liu, J. Zhang, J. Mao, J. Wang, X. Han, Y. Deng, W. Hu, Reconstructed bismuth oxide through in situ carbonation by carbonate-containing electrolyte for highly active electrocatalytic CO_2 reduction to formate, Angew. Chem. Int. Ed. 63 (2023) e202316640.
[21] M. Wang, H. Chen, M. Wang, J. Wang, Y. Tuo, W. Li, S. Zhou, L. Kong, G. Liu, L. Jiang, G. Wang, Tuning C_1/C_2 selectivity of CO_2 electrochemical reduction over in-situ evolved CuO/SnO_2 heterostructure, Angew. Chem. Int. Ed. 62 (2023) e202306456.
[22] Q. Zhang, M. Sun, C.-Y. Yuan, Q.-W. Sun, B. Huang, H. Dong, Y.-W. Zhang, Strong electronic coupling effects at the heterojunction interface of SnO_2 nanodots and g-C_3N_4 for enhanced CO_2 electroreduction, ACS Catal. 13 (2023) 7055–7066.
[23] J. Yang, X. Wang, Y. Qu, X. Wang, H. Huo, Q. Fan, J. Wang, L.-M. Yang, Y. Wu, Bi-based metal-organic framework derived leafy bismuth nanosheets for carbon dioxide electroreduction, Adv. Energy Mater. 10 (2020) 2001709.
[24] S. Ning, J. Wang, D. Xiang, S. Huang, W. Chen, S. Chen, X. Kang, Electrochemical reduction of SnO_2 to Sn from the bottom: in-situ formation of SnO_2/Sn heterostructure for highly efficient electrochemical reduction of carbon dioxide to formate, J. Catal. 399 (2021) 67–74.
[25] Y. Zhang, S. Liu, N. Ji, L. Wei, Q. Liang, J. Li, Z. Tian, J. Su, Q. Chen, Modulation of the electronic structure of metallic bismuth catalysts by cerium doping to facilitate electrocatalytic CO_2 reduction to formate, J. Mater. Chem. A 12 (2024) 7528–7535.
[26] Y. Shi, Y. Wang, J. Yu, Y. Chen, C. Fang, D. Jiang, Q. Zhang, L. Gu, X. Yu, X. Li, H. Liu, W. Zhou, Superscalar phase boundaries derived multiple active sites in SnO_2/Cu_6Sn_5/CuO for tandem electroreduction of CO_2 to formic acid, Adv. Energy Mater. 13 (2023) 2203506.
[27] Y. Zhao, X. Liu, Z. Liu, X. Lin, J. Lan, Y. Zhang, Y.-R. Lu, M. Peng, T.-S. Chan, Y. Tan, Spontaneously Sn-doped Bi/BiO_x core-shell nanowires toward high-performance CO_2 electroreduction to liquid fuel, Nano Lett. 21 (2021) 6907–6913.

[28] H. Jiang, Z. Fan, M. Zhang, S. Guo, L. Li, X. Yu, Z. Liu, W. Wang, H. Dong, M. Zhong, Redox-stabilized Sn/SnO_2 nanostructures for efficient and stable CO_2 electroreduction to formate, ChemElectroChem 10 (2023) e202201164.
[29] A. Dutta, A. Kuzume, M. Rahaman, S. Vesztergom, P. Broekmann, Monitoring the chemical state of catalysts for CO_2 electroreduction: an in operando study, ACS Catal. 5 (2015) 7498–7502.
[30] S. Gao, Y. Lin, X. Jiao, Y. Sun, Q. Luo, W. Zhang, D. Li, J. Yang, Y. Xie, Partially oxidized atomic cobalt layers for carbon dioxide electroreduction to liquid fuel, Nature 529 (2016) 68–71.
[31] Z. Wu, L. Yan, T. Lu, H. Wang, C. Wang, Y. Guo, H. Wen, Z. Zhao, C. Wang, Q. Guo, J. Wang, One-pot synthesis of surfactant-intercalated tin(IV) disulfide nanosheets heterojuncted with bismuth(III) sulfide needles for efficient conversion carbon dioxide into formate, J. Colloid Interface Sci. 687 (2025) 36–47.
[32] X. Wang, Y. Zou, Y. Zhang, B. Marchetti, Y. Liu, J. Yi, X.-D. Zhou, J. Zhang, Tin-based metal organic framework catalysts for high-efficiency electrocatalytic CO_2 conversion into formate, J. Colloid Interface Sci. 626 (2022) 836–847.
[33] X. Yang, P. Deng, D. Liu, S. Zhao, D. Li, H. Wu, Y. Ma, B.Y. Xia, M. Li, C. Xiao, S. Ding, Partial sulfuration-induced defect and interface tailoring on bismuth oxide for promoting electrocatalytic CO_2 reduction, J. Mater. Chem. A 8 (2019) 2472–2480.
[34] Z. Niu, X. Gao, S. Lou, N. Wen, J. Zhao, Z. Zhang, Z. Ding, R. Yuan, W. Dai, J. Long, Theory-guided S-defects boost selective conversion of CO_2 to HCOOH over In_4SnS_8 nanoflowers, ACS Catal. 13 (2023) 2998–3006.
[35] Y. Lv, Z. Yu, S. Huang, F. Deng, K. Zheng, G. Yang, Y. Liu, C. Lin, X. Ye, M. Liu, Rapidly photocatalytic mineralization of typical veterinary drugs with the SnO_2/$SnIn_4S_8$ composite, Chemosphere 271 (2021) 129452.
[36] N. Wang, C. Shao, R. Zhang, Y. Zhang, Z. Min, B. Chang, M. Fan, J. Wang, Metal-organic framework derived Bi-O-Sn/C nanostructure: tailoring the adsorption site of dominant intermediate for highly efficient CO_2 electroreduction to formate, Small 20 (2023) 2306129.
[37] F. Liu, J. Wang, X. Ren, H. Wu, J. Zhao, J. Zhang, W. Xie, G. Wang, X. Han, Y. Deng, W. Hu, In-situ reconstructed In doped SnO_2 amorphous–crystalline heterostructure for highly efficient CO_2 electroreduction with a dynamic structure-function relationship, Appl. Catal. B: Environ. 352 (2024) 124004.
[38] H. Shen, H. Jin, H. Li, H. Wang, J. Duan, Y. Jiao, S.-Z. Qiao, Acidic CO_2-to-HCOOH electrolysis with industrial-level current on phase engineered tin sulfide, Nat. Commun. 14 (2023) 2843.
[39] C. Song, K. Jiang, P. Shi, X. Chai, J. Zhang, C. Lu, Y. Su, X. Zhuang, T. Wang, Interfacial engineering of bismuth sulfide/oxychloride heterostructure for boosting the conversion from CO_2 to formate at large current densities, Chem. Eng. Sci. 277 (2023) 118838.
[40] V.G. Rao, U. Aslam, S. Linic, Chemical requirement for extracting energetic charge carriers from plasmonic metal nanoparticles to perform electron-transfer reactions, J. Am. Chem. Soc. 141 (2018) 643–647.
[41] G. Wen, D.U. Lee, B. Ren, F.M. Hassan, G. Jiang, Z.P. Cano, J. Gostick, E. Croiset, Z. Bai, L. Yang, Z. Chen, Orbital interactions in Bi-Sn bimetallic electrocatalysts for highly selective electrochemical CO_2 reduction toward formate production, Adv. Energy Mater. 8 (2018) 1802427.
[42] Z. Wei, J. Ding, Z. Wang, A. Wang, L. Zhang, Y. Liu, Y. Guo, X. Yang, Y. Zhai, B. Liu, Enhanced electrochemical CO_2 reduction to formate over phosphate-modified In: water activation and active site tuning, Angew. Chem. Int. Ed. 63 (2024) e202402070.
[43] G. Xing, S. Liu, J.-Y. Liu, Two-dimensional metal-organic frameworks with dual active sites for electrochemical CO_2 reduction: a computational study, Sep. Purif. Technol. 361 (2025) 131275.